Journal of Materials Chemistry A

ROYAL SOCIETY OF CHEMISTRY

PAPER

View Article Online
View Journal | View Issue

Check for updates

Cite this: J. Mater. Chem. A, 2025, 13, 15762

Controllable dispersion of nickel phthalocyanine molecules on graphene oxide for efficient electrocatalytic CO_2 reduction†

Jiaxin He,[abd] Yu Han,[abd] Xiao Xu,[bd] Miao Sun,[bd] Longtian Kang, *[abd] Wenlie Lin*[b] and Jingjing Liu*[c]

Received 27th February 2025
Accepted 2nd April 2025

DOI: 10.1039/d5ta01623a

rsc.li/materials-a

Single-atom electrocatalysts with Ni–N_x–C sites usually possess excellent activity for the CO_2 reduction reaction (CO_2RR). However, it still remains a challenge to synthesize them using unmodified nickel phthalocyanine (NiPc) with an intrinsic Ni–N_4–C moiety at room temperature. Here, NiPc molecules are controllably dispersed on graphene oxide (GO) in the form of single molecules, dimers, or aggregates through a simple hydrolysis of protonated NiPc in a GO-containing aqueous phase. Systematic characterization shows the existence of π–π interaction, hydrogen bond and axial coordination between NiPc and GO in NiPc–GO composites. Electrochemical tests demonstrate that these NiPc–GO composites have high activity for electrocatalytic CO_2RR to CO. After optimizing the GO content in NiPc–GO, a CO Faraday efficiency of >90% is achieved over a work potential range of −0.8 to −1.1 V_{RHE}, reaching up to 98.6% at −0.9 V_{RHE}. Further experiments confirm that GO in NiPc–GO benefits CO_2 adsorption and formation of the *COOH intermediate. The change in the Ni^{2+}/Ni^{3+} ratio with the GO amount in NiPc–GO composites reveals that the Ni(II)/Ni(III)/GO heterojunction structure is the most conductive to the CO_2RR process. This work provides an insight into the design and synthesis of single-atom Ni–N_4–C electrocatalysts for the CO_2RR.

1. Introduction

In recent years, the global energy crisis and environmental challenges have become increasingly severe. The excessive consumption of traditional fossil fuels has led to a surge in greenhouse gas emissions, contributing to global warming and ecological issues.[1] Hence, the study on reducing and recycling CO_2 has attracted increasing attention.[1–4] The electrochemical CO_2RR technology can offer an efficient and sustainable route to convert CO_2 into high-value chemicals and fuels under mild conditions. Therefore, it is considered as one of promising strategies to achieve carbon neutrality. Up to date, a variety of products, such as carbon monoxide (CO), methane (CH_4), ethylene (C_2H_4), and ethanol (C_2H_5OH), have been synthesized by designing catalysts and optimizing reaction conditions.[3,5–8] These products can act as alternative fuels to replace traditional fossil energy sources and serve as raw materials for the industrial production of high-value items, thus supporting the advancement of a sustainable energy system. The CO_2RR involves a complicated process. The stability and the product selectivity usually depend on the structure and electronic properties of catalysts, the reaction environment, *etc.*[9] An ideal material for electrocatalytic CO_2RR should possess the ability for efficient CO_2 adsorption, suitable adsorption/desorption for different intermediates, high conductivity, fully exposed active sites on the surface, *etc.* Unfortunately, few single-component materials can meet the above conditions simultaneously. Recently, noble metal catalysts, *e.g.* Au, Ag, Pd, *etc.*, have been widely investigated in CO_2RR research due to their excellent catalytic performance.[10–12] Usually, the active sites of Au and Ag sites can exhibit high CO selectivity, while the Pd site can promote the conversion of CO_2 into complex hydrocarbons. However, the high-cost, scarcity, and potential stability issues of noble metal catalysts severely limit their industrial application.[13] Therefore, it is urgent to explore more economic catalysts with high stability and activity. In the past decade, the materials with a metal–nitrogen–carbon (M–N_x–C) structure have attracted significant attention because of their intrinsic and stable single-atom sites and low cost.[14–17] In recent years, significant progress has been made in the design and synthesis of M–N_x–C single-atom electrocatalysts (SACs) for CO_2RR, especially, the

[a]College of Chemistry, Fuzhou University, Fuzhou 350116, PR China
[b]State Key Laboratory of Structural Chemistry, Fujian Provincial Key Laboratory of Nanomaterials, Fujian Institute of Research on the Structure of Matter, Chinese Academy of Sciences, Fuzhou, Fujian 350002, PR China
[c]Fujian Universities and Colleges Engineering Research Center of Soft Plastic Packaging Technology for Food, Fujian Polytechnic Normal University, Fuqing, Fujian Province, 350300, PR China
[d]University Chinese Academy of Science, Fujian College, Fuzhou 350002, PR China. E-mail: longtiank@fjirsm.ac.cn

† Electronic supplementary information (ESI) available. See DOI: https://doi.org/10.1039/d5ta01623a

Fe, Co and Ni-based SACs.[2,3,18–23] The Ni SACs usually have higher selectivity for CO than Fe- or Co-SACs owing to the weaker adsorption ability of the Ni central atom for the *CO intermediate.[24] For example, Wang *et al.*[25] synthesized Ni SACs with an asymmetric Ni–X–N_3–C structure *via* pyrolysis, and achieved a CO faradaic efficiency (FE_{CO}) of 98% at −0.70 V *versus* the reversible hydrogen electrode (*vs.* RHE). The NiPc/N-mG (900) catalyst prepared at high temperature exhibits excellent performance, achieving a FE_{CO} of >90% in the potential range of −0.5 to −1.1 V *vs.* RHE, and a FE_{CO} of 96.4% and a J_{CO} of −7.8 mA cm^{-2} at −0.9 V *vs.* RHE.[26]

In fact, M–N_x–C SACs can be easily synthesized through the pyrolysis of a mixture of metal, nitrogen and carbon precursors at high temperature. Meanwhile, recent studies have revealed that Ni–N_3 or Ni–N_4 sites may have higher activity for CO_2RR as active sites.[2,15] However, the high-temperature pyrolysis synthesis method frequently leads to the presence of multiple Ni–N_x ligands, complicating the identification of the true active sites and hindering a deeper understanding of the catalytic mechanism.[26] Recently, nickel phthalocyanine (NiPc) with a well-defined Ni–N_4–C moiety has also garnered significant attention in the electrocatalytic reduction process as a catalyst.[27–30] However, NiPc molecules suffer from low electron density at the Ni site, weakening their ability to adsorb and activate CO_2.[27] What's worse, the strong intermolecular π–π interaction easily results in the formation of J-type or H-type aggregates with low conductivity,[31] and then reduces the exposure of Ni–N_4–C sites on the surface. To address these issues, a popular strategy is to modify NiPc with amino, cyano, methoxy, *etc.* groups,[18,29,32] and then disperse them on carbon substrates.[31] Unfortunately, there have been few reports on the controlled dispersion of unmodified NiPc molecules so far. In this work, we provide a simple method to synthesize carbon-based NiPc composites through the hydrolysis of protonated NiPc in a GO-containing aqueous phase at room temperature. The dispersion forms of NiPc molecules from aggregates, dimers, and single molecules can be clearly observed on GO with the increase in GO amount in the NiPc–GO composites. A series of characterization studies revealed the interactions between NiPc and GO. After optimizing the mass ratio of NiPc to

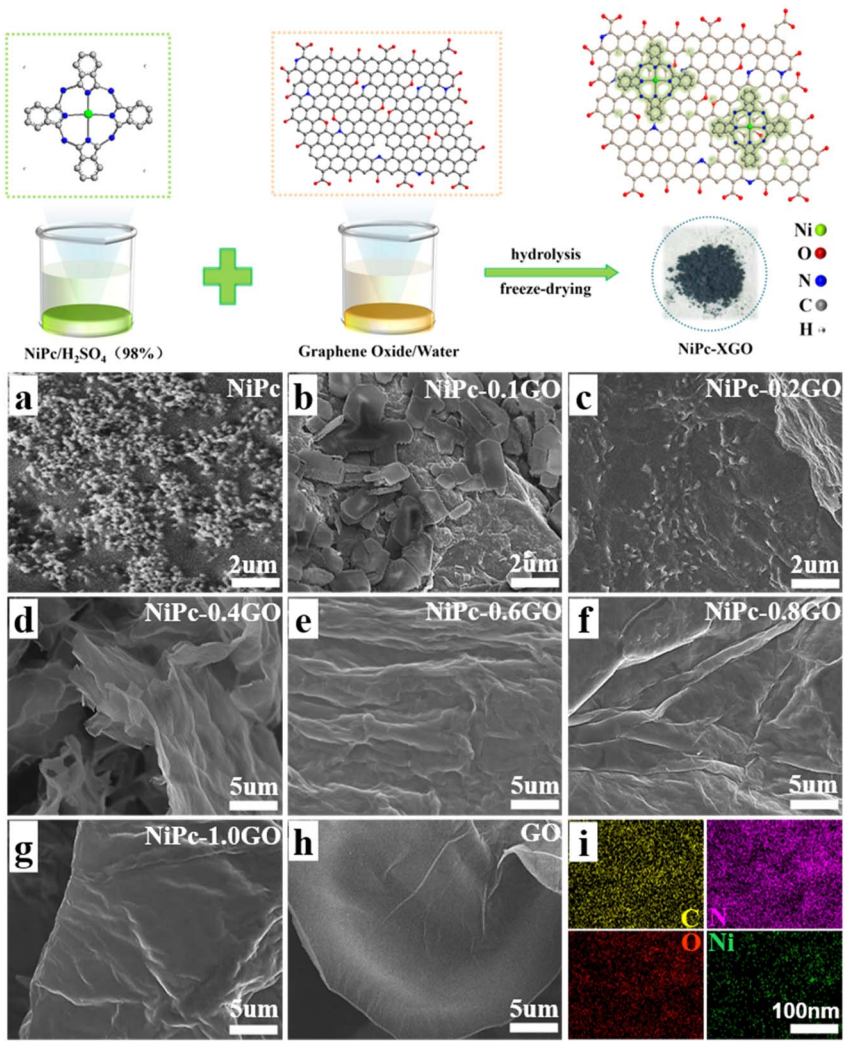

Fig. 1 Schematic illustration of the synthesis of NiPc/GO composites. SEM images of (a) NiPc, (b) NiPc−0.1GO, (c) NiPc−0.2GO, (d) NiPc−0.4GO, (e) NiPc−0.6GO, (f) NiPc−0.8GO, (g) NiPc−1.0GO, and (h) GO. (i) Elemental mappings of C, N, O, and Ni atoms.

GO, a FE_{CO} of 98.6% can be achieved at −0.9 V *vs.* RHE, and a FE_{CO} of >90% can be maintained across the potential range of −0.7 to −1.0 V *vs.* RHE. Furthermore, *in situ* diffuse reflectance infrared Fourier-transform spectroscopy (DRIFTS) confirmed the synergistic mechanism between NiPc and GO for CO_2RR to CO. This work provides an efficient way to design the Ni–N_4–C electrocatalyst and deeply understand the role of NiPc dimers and GO in the CO_2RR.

2. Results and discussion

As shown in Fig. 1, the NiPc–GO composites were synthesized through the hydrolysis of protonated NiPc in a GO-containing aqueous phase. In a typical process, 1.0 mL of 1.0 mM NiPc/H_2SO_4 (98%) solution was added into 5.0 mL of an aqueous GO dispersion. The as-obtained samples were labeled as NiPc–*x*GO, where *x* represents the solid content of GO in water (mg mL^{-1}). The detailed process can be found in the ESI.† All samples were first characterized using scanning electron microscopy (SEM) and elemental mapping to investigate their size, morphology and components. Fig. 1a shows the presence of numerous micron particles with irregular surfaces in the pure NiPc sample. Fig. 1b–g and S1–S6† illustrate the morphological changes of NiPc–GO composites with the increase in GO solid content from 0.1 to 1.0 mg mL^{-1} in the synthesis system. Fig. 1b and S1† reveal that upon the introduction of 0.1 mg mL^{-1} GO, two-dimensional (2D) structures begin to emerge, demonstrating the templating role of GO in directing the crystal growth.[33] When the GO amount is increased to 0.2 mg mL^{-1}, only a small number of nanoparticles form on the GO surface, and the profile of the 2D structure becomes clearer in NiPc–0.2GO (see Fig. 1c and S2†). Surprisingly, as shown in Fig. 1d and S3†, with the increase in GO amount to 0.2 mg mL^{-1}, no obvious nanoparticles can be observed in NiPc–0.4GO; meanwhile, the 2D structure appears clearer and its rigidity is significantly enhanced. When the GO amount is further increased from 0.4 to 0.6, 0.8 and 1.0 mg mL^{-1}, Fig. 1e–g and S4–S6† reveal that not only nanoparticles disappear, but also the 2D structure becomes smoother resembling typical GO shown in Fig. 1g. The elemental mappings of C, O, Ni, and N atoms in NiPc–0.4GO prove that Ni and N atoms in NiPc are evenly distributed in the 2D structure, and are consistent with those of C and O atoms in GO (see Fig. 1i and S7†). The above phenomena strongly suggest that NiPc can be adequately dispersed on GO in NiPc–GO when an appropriate GO amount is used. To gain insight into the distribution evolution of NiPc molecules on the GO surface with the increase in GO content in NiPc–GO, high-angle annular dark-field scanning transmission electron microscopy (HADDF-STEM) was performed to observe the NiPc–0.4GO, NiPc–0.6GO and NiPc–0.8GO samples. In the high-resolution HADDF-STEM images shown in Fig. 2a–c and S8–S10,† the tiny bright spots represent Ni atoms on the GO surface. Because HADDF-STEM images reveal a two-dimensional projection along the incident beam direction, the characteristics of atomically dispersed Ni atoms differ slightly in three-dimensional space.[34] The distribution density of bright

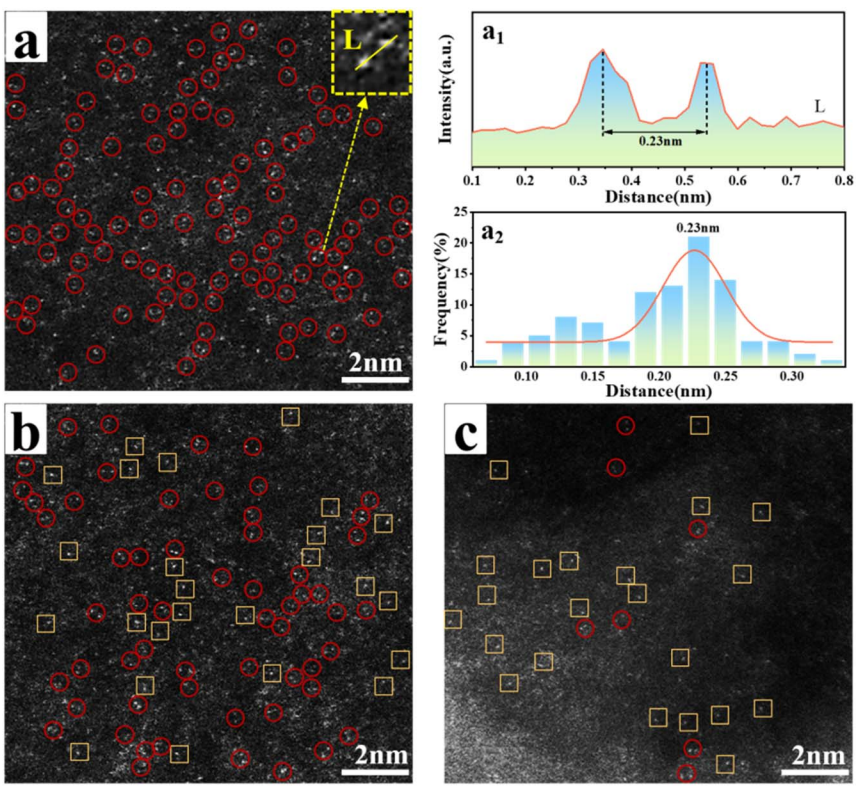

Fig. 2 HADDF-STEM images of (a) NiPc–0.4GO, (b) NiPc–0.6GO, and (c) NiPc–0.8GO samples. (a_1) Intensity profiles along the arrows and (a_2) Ni–Ni distance distribution of NiPc–0.4GO.

spots reflects the amount of NiPc on GO, while differences in their brightness and size indicate the distance of NiPc molecules from the surface. Hence, the Ni atoms should be sufficiently dispersed in the three samples. In Fig. 2a and S8,† some regions show the accumulation of Ni atoms, suggesting the presence of NiPc aggregates on GO within the NiPc–0.4GO sample. Interestingly, many atomic pairs of Ni atoms are also observed, as labeled with red circles. Meanwhile, one spot is brighter than the other. The corresponding statistical results show that the average distance between two spots in an atomic pair is 2.3 Å, which is much smaller than the 1.37-nm size of a NiPc molecule.[35] These results clearly verify that a large number of NiPc dimers are formed in NiPc–0.4GO, indicating the generation of a NiPc/NiPc/GO structure. When the GO amount is raised to 0.6 mg mL^{-1}, the number of Ni atomic pairs decreases, while the single-atom sites of Ni labeled with yellow circles begin to appear within the NiPc–0.6GO sample, as shown in Fig. 2b and S9†. Fig. 2c and S10† reveal that in the NiPc–0.8GO sample, the NiPc dimers nearly disappear, and the single NiPc molecules become more prominent and are uniformly distributed on GO. These experimental results sufficiently confirm that with the increase in GO from 0.4 to 0.8 mg mL^{-1}, NiPc molecules exist on GO, and their form changes from aggregates and dimers to single molecules on GO. The observed evolution of NiPc morphology on GO indicates that besides the π–π interaction between GO and NiPc, other strong interactions should exist to overcome the intermolecular interaction of NiPc. Noteworthy, the so-called NiPc aggregates observed on GO in HADDF-STEM images are an illusion, likely resulting from the folding and twisting of GO.

Combining the experimental results from SEM, elemental mapping, and HADDF-STEM characterization, we can conclude that unmodified NiPc molecules can be adequately dispersed on GO in various forms by adjusting the ratio of GO to NiPc during the hydrolysis process of protonated NiPc. These NiPc–GO composites provide a solid foundation for the study of NiPc-based CO_2RR. To further reveal the structure of NiPc–GO composites and the interactions between NiPc and GO, X-ray diffraction (XRD), Raman spectroscopy, Fourier transform infrared spectroscopy (FT-IR), and X-ray photoelectron spectroscopy (XPS) spectra of NiPc, GO, and NiPc–0.4GO samples were measured and carefully analyzed. The XRD patterns in Fig. 3a clearly display the typical (001) facet peak of GO at 10.21°, corresponding to an interlayer distance of 0.87 nm.[36] The diffraction peak of the NiPc sample at 6.41° can be assigned to the (100) facet of the NiPc crystal.[37] Compared to pure NiPc samples, the XRD peaks of NiPc and GO disappear in NiPc–0.1GO, replaced by three broad, diffuse peaks of NiPc aggregates.[38] As the GO concentration increases from 0.1 to 1.0 mg mL^{-1}, the XRD peaks of NiPc aggregates in NiPc–GO composites decrease sharply and vanish within the 20–30° range. These changes directly reflect the dispersion process of NiPc molecules on the GO surface, agreeing with the SEM results. Additionally, it can be found that with increasing GO content in the NiPc–GO sample, the XRD peak of NiPc dimers gradually weakens at ~7°, meanwhile, a weak XRD peak starts appearing at ~9° in NiPc–0.4GO, which gradually intensifies, and shifts to lower angles. This phenomenon indicates the formation of a new ordered structure between NiPc and GO in NiPc–GO composites, suggesting that the NiPc molecules may be embedded within the GO interlayers, as shown in Fig. 1 and 2. The Raman spectrum of NiPc–0.4GO in Fig. 3b exhibits two clear peaks at 1346.5 and 1640.7 cm^{-1}, corresponding to the D and G bands of carbon materials, respectively.[39] The D band reflects defects and disorder in sp^2 carbon rings, while the G band is associated with the C–C/C=C tangential stretching mode. Compared to pure GO, the D band of NiPc–0.4GO red-shifts and the G band blue-shifts. The I_D/I_G ratio increases from 0.97 in GO to 1.01 in NiPc–0.4GO, suggesting that the GO in the NiPc–0.4GO composite likely contains new defects or

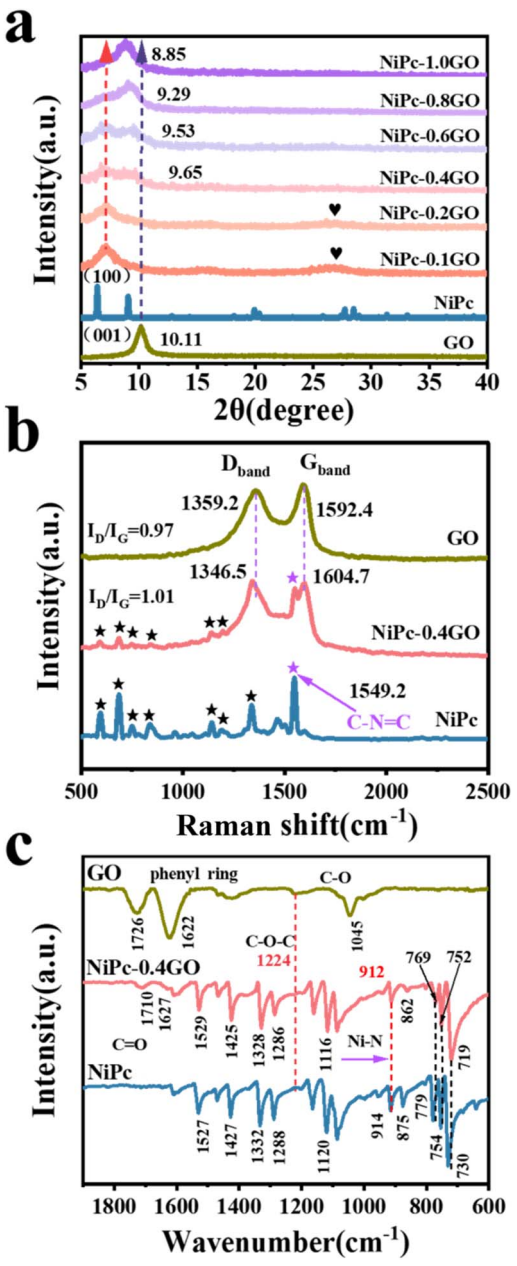

Fig. 3 (a) XRD patterns of GO and NiPc–GO composites. (b) Raman spectra and (c) FT-IR spectra of NiPc, GO, and NiPc–0.4GO samples.

structural distortions. Compared to pure NiPc, NiPc in NiPc–0.4GO shows a distinct vibration peak of the C–N=C bond at 1549.2 cm^{-1}, while other peaks are significantly weaker. These Raman spectral changes of NiPc and GO in NiPc–GO composites indicate the existence of other strong interactions besides π–π interaction between NiPc and GO in NiPc–GO, which alter the structures and vibration models of graphene and NiPc.[33,40]

The FT-IR spectra of NiPc, GO, and NiPc–0.4GO samples are investigated, as shown in Fig. 3c. The characteristic vibration peaks of NiPc molecules appear at 914, 1085, 1120, 730, 754 and 779 cm^{-1}, corresponding to the stretching vibrations of Ni–N, pyridine C–N and pyrrole C–N bonds, and the bending vibration of C–H bonds.[30,36,41] The characteristic peaks of GO can be observed at 1224 and 1726 cm^{-1}, which arise from the stretching vibration of C–O–C and C=O bonds.[40] In the NiPc–0.4GO composite, the characteristic vibration peaks of NiPc and GO are still present, indicating the successful recombination between NiPc and GO. However, three interesting phenomena can be found in the FT-IR spectrum of NiPc–GO, as compared to those of GO and NiPc. (1) The stretching vibration peaks of the benzene ring backbone shift from 1622 and 1527 cm^{-1} to 1627 and 1529 cm^{-1}.[40,42] It means that the π–π interaction between GO and NiPc has been enhanced, resulting in the planarity enhancement of conjugated rings. (2) The C=O vibration peak of GO in NiPc–0.4GO at 1726 cm^{-1} increases by 16 cm^{-1}, as compared to that of pure GO (1710 cm^{-1}), and the bending vibration peaks of C–H bond decrease from 779 and 730 $cm^{-1}$to 769 and 719 cm^{-1}. This suggests that the hydrogen bonding may form between the C=O bond of GO and the C–H bond of NiPc in NiPc–GO. In the NiPc–0.4GO composite, the peak intensity of the C–O–C bond at 1224 cm^{-1} decreases significantly, indicating the cleavage of the C–O–C bond owing to coordination with the central Ni atom of NiPc.[40,41] Consequently, the coordination changes of Ni result in the decrease of the vibration peak of the phthalocyanine ring at 914 cm^{-1} and the C–N peak at 1120 cm^{-1} by 2 and, 4 cm^{-1}, respectively. Therefore, there should be strong hydrogen bonds and axial coordination bonds besides the π–π interaction between GO and NiPc in the NiPc–GO composites.

To further investigate the interaction between NiPc and GO, the XPS spectra of GO, NiPc, and NiPc–0.4GO samples were measured to carefully study the changes in the chemical environment of C, N, O and Ni atoms, as displayed in Fig. 4 and S12.† The appearance of C 1s, N 1s, O 1s and Ni 2p peaks in the XPS full spectra of NiPc–0.4GO sample confirms the formation of the GO–NiPc composite (see Fig. S12†).[43] In Fig. 4a, the high-resolution Ni 2p XPS spectra of NiPc and NiPc–0.4GO samples exhibit a pair of relatively narrow spin–orbit characteristic doublets. For NiPc, the peaks at 872.2 and 855.1 eV can be assigned to Ni $2p_{1/2}$ and Ni $2p_{3/2}$ of Ni^{2+}.[44,45] Compared with NiPc, the XPS peaks of Ni^{3+} can be identified at 855.9 eV (Ni^{3+} $2p_{3/2}$) and 873.2 eV (Ni^{2+} $2p_{1/2}$) in the NiPc–0.4GO composite,[44–46] indicating a decrease in electron cloud density around the Ni atoms.[27] The high-resolution N 1s XPS spectrum in Fig. 4b shows that as compared to NiPc, the binding energy of pyrrole nitrogen (Ni–N) reduces from 400.2 to 399.9 eV in NiPc–0.4GO, while the binding energy of pyridine nitrogen (C–N) remains at 398.6.[30,41] Here, the graphite C–N peak at 401.5 eV in

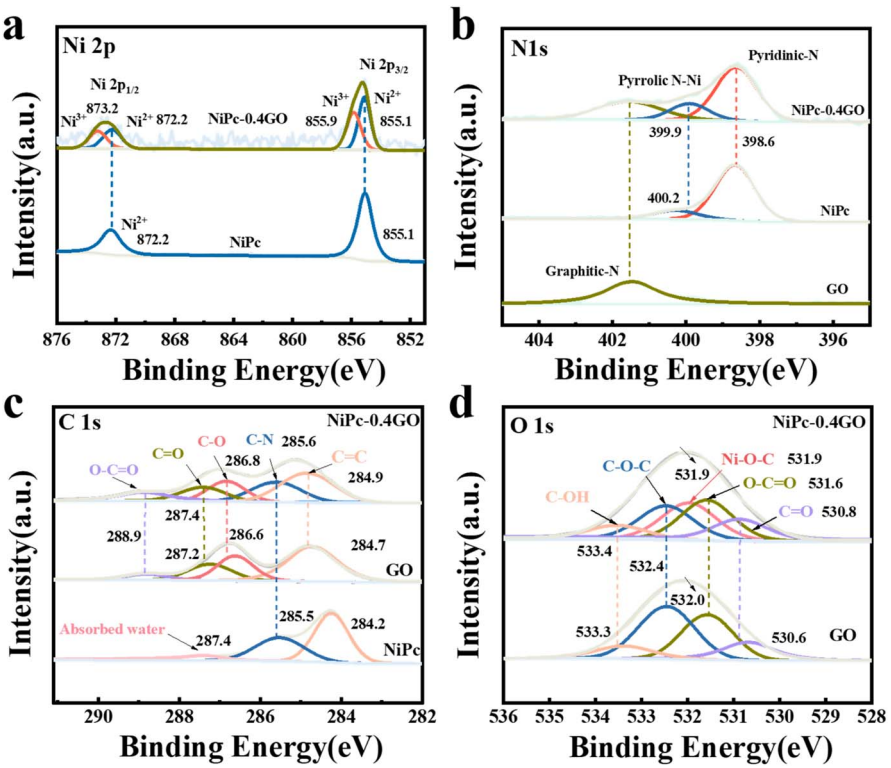

Fig. 4 (a–d) High-resolution XPS spectra of (a) Ni 2p, (b) N 1s, (c) C 1s, and (d) O 1s of NiPc, GO, and NiPc–0.4GO samples.

GO likely originates from the residual reactant remaining from the synthesis process of GO. The binding energy changes of Ni 2p and N 1s in the Ni–N bond demonstrate the reduction of the Ni–N bond length and the planarity enhancement of the NiPc molecule in NiPc–0.4GO owing to the change in the coordination number of surface Ni atoms from five-coordination to six-coordination.[40,41] As shown in Fig. 4c, the high-resolution C 1s XPS spectra can be deconvoluted into five components: C–C/C=C, C–N, C–OH, –O–C=O and C=O bonds.[47–49] In the NiPc–0.4GO composite, the binding energy of the –O–C=O bond in GO remains at 288.9 eV. However, the C 1s binding energies of the C=C (284.7 eV), C–OH (286.6 eV) and C=O (287.2 eV) bonds in GO each increase by 0.2 eV in NiPc–0.4GO. The results suggest that the sp^2-C electrons are transferred from GO to NiPc through the π–π interaction. In the high-resolution XPS spectra of O 1s shown in Fig. 4d, four typical peaks of C=O (530.6), O–C=O (531.6 eV), C–O–C (532.4 eV), and C–OH (533.3 eV) can be identified in GO.[40,50] Here, the overall binding energy of O 1s is lower in NiPc–0.4GO than that in GO (532.0 *vs.* 531.9 eV). However, the binding energies of C–OH (533.4 *vs.* 533.3 eV) and C=O (530.8 *vs.* 530.6 eV) bonds in NiPc–0.4GO are higher than those in GO. In addition, it can be found that in NiPc–0.4GO, the content of the C –O–C bond at 532.4 eV decreases and a new peak corresponding to the C–O–Ni bond appears at 531.9 eV.[33] This indicates the axial coordination of the central Ni atom in Ni–N_4 with the C–O group, leading to the formation of the Ni(II)Pc/Ni(III)Pc/GO structure.[41,51] The increase in binding energies of the C 1s and O 1s peaks of both C–OH and C=O bonds in NiPc–GO indicates that the hydrogen bonds may exist between the C–O/C=O bond in GO and the C–H bond in NiPc. This may explain why the bending vibration of the C–H bond in NiPc becomes weaker in NiPc–GO (see Fig. 3c). Based on the above XPS results, we can conclude that the interactions between GO and NiPc in the NiPc–GO composites can be assigned to the π–π interaction, the hydrogen bond and the C–O–Ni axial coordination bond. As a result, the NiPc molecules can be controllably dispersed on GO during the synthesis process of NiPc–GO composites.

3. Electrocatalytic performance of NiPc/GO for the CO_2RR

Here, the electrocatalytic CO_2RR activity of the as-obtained samples as catalysts is evaluated in an H-type electrolysis cell, with CO_2-saturated 0.1 M $KHCO_3$ solution as the electrolyte (see Fig. 5). In our test, only gaseous products of CO and H_2 can be detected. Fig. 5a shows the LSV curves of NiPc, GO and NiPc–0.4GO samples in CO_2-saturated and Ar-saturated solutions. Obviously, these samples exhibit higher current densities (J_{total}) and onset potentials in CO_2-saturated solution, confirming their CO_2RR activity. The more negative J_{total} generated with NiPc–0.4GO as the catalyst indicates that the synergy between NiPc and GO is beneficial for the CO_2RR process. Fig. 5b presents the J_{total} change of NiPc–GO composites with work potential. It can be found that with the increase in GO amount from 0.1 to 1.0 mg mL^{-1}, the J_{total} first increases, and then decreases. As usual, this phenomenon arises from the competing effects of catalyst dispersion/aggregation and the uneven distribution density of active sites on the substrate.[40] Both the formation of NiPc aggregates and a low distribution density of NiPc on GO are unfavorable for the CO_2RR. Among them, the NiPc–0.4GO sample exhibits the best activity for the CO_2RR. Fig. 5c also proves that the CO current density (J_{CO}) of NiPc–0.4GO is the highest, reaching up to –8.5 mA cm^{-2} at –1.0 V (*vs.* RHE). In Fig. 5d and Table S1,† the effect of the GO amount in NiPc–GO composites on FE_{CO} is systematically recorded at different work potentials. It can be found that the FE_{CO} order is NiPc–0.4GO > NiPc–0.2GO > NiPc–0.1GO, and NiPc–0.4GO > NiPc–0.6GO > NiPc–0.8GO > NiPc–1.0GO. In the potential range of –0.6 to –1.1 V (*vs.* RHE), the FE_{CO} of all samples shows a volcano-like trend. The highest FE_{CO} of 98.6% can be achieved at –0.9 V (*vs.* RHE) with NiPc–0.4GO as the catalyst, and a FE_{CO} of > 90% can be obtained in the potential range of –0.7 to –1.0 V (*vs.* RHE). Hence, the CO_2RR activity of NiPc–GO composite can be easily optimized by changing the mass ratio of NiPc to GO during the synthesis process of NiPc–GO. Combining with the XRD results in Fig. 3a and the HADDF-STEM results in Fig. 2, these changes strongly reveal that the Ni–N_4 group is the indeed active site for CO_2RR, and the Ni(II)Pc/Ni(III)Pc/GO structure performs better than the single-atom NiPc–GO structure for CO_2RR, even if the number of exposed Ni–N_4 sites on the surface is the same on GO in NiPc–0.6GO and NiPc–0.8GO samples. Compared to previous reports on carbon-based Ni–N_x–C catalysts for CO_2RR, our work not only offers a simpler method but also achieves optimal FE_{CO} with the lowest loading density of active sites, as listed in Table S2.† Fig. 5e proves that after the CO_2RR test for 6 hours at –0.9 V (*vs.* RHE), the NiPc–0.4GO material still maintains a FE_{CO} of >95%, confirming its outstanding stability.

To further investigate the stability of NiPc–0.4GO, its CV curves, SEM images, XRD pattern, and FT-IR, Raman and XPS spectra were characterized after the test, as seen Fig. 5f and S14–S17.† The post-reaction CV curve in Fig. 5f shows that the CV area remains unchanged before/after the test, indicating that the number of active sites in NiPc–0.4GO remains the same. Surprisingly, the oxidation and reduction regions show better symmetry after the test, indicating that the electrochemical reversibility is improved. SEM images in Fig. S14† demonstrate that the NiPc–0.4GO sample retains its original sheet-like morphology after the test. No particles of NiPc can be found on GO. The increase in GO aggregation suggests the partial reduction of GO in the NiPc–GO composite during the test. The XRD spectra in Fig. S15† show that after the test, the characteristic peaks of NiPc and the (002) peak of GO remain unchanged. Meanwhile, no broad diffuse peaks corresponding to NiPc aggregates emerge, confirming that the molecular dispersion of NiPc on GO surfaces is stable during the prolonged electrochemical test. As shown in Fig. S16a,† the FT-IR spectra of NiPc–0.4GO obtained after the test exhibit preserved vibrational peaks assigned to NiPc, including Ni–N (912 cm^{-1}), pyridinic C–N (1085 cm^{-1}), and pyrrolic C–N (1116 cm^{-1}), and the strong skeletal vibration of the phthalocyanine ring (719 cm^{-1}). However, the intensity of the C=O

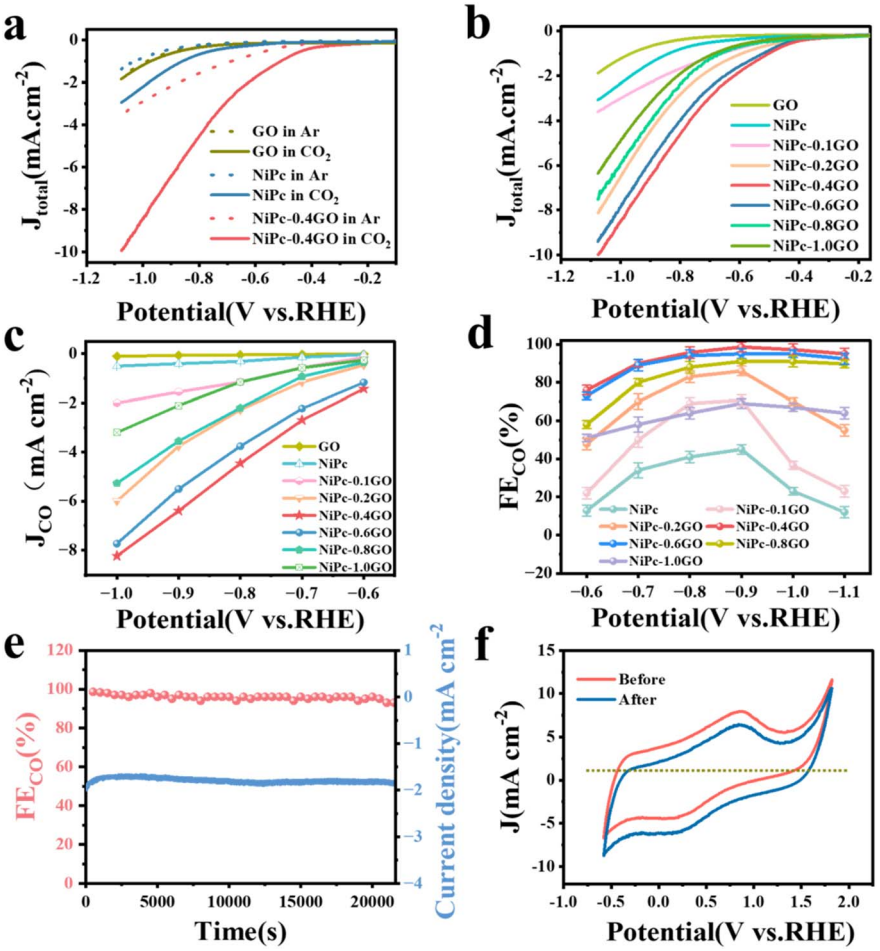

Fig. 5 Electrocatalytic CO_2RR performance in a CO_2-saturated 0.1 M $KHCO_3$ solution. (a) LSV curves of GO, NiPc, and NiPc–0.4GO in Ar-and CO_2-saturated electrolytes. (b) J_{total} and (c) J_{CO} of GO, NiPc and NiPc–GO composites at different work potentials. (d) FE_{CO} change of NiPc and NiPc–GO samples at different work potentials. (e) Chronoamperometric curve and the corresponding FE_{CO} of NiPc–0.4GO during a 6-hour test at −0.9 V (*vs.* RHE). (f) CV curves of NiPc–0.4GO after/before the test.

double bond (1720 cm^{-1}) significantly increases, which can be attributed to the chemical adsorption of corresponding intermediates on the catalyst surface. Fig. S16b† confirms that the Raman spectra before and after the reaction are consistent, demonstrating the stability of the NiPc structure under electrocatalytic conditions. However, the I_D/I_G ratio declines from 1.01 to 0.99, suggesting that a decrease in the defects of sp^2-C due to the unavoidable reduction of GO. XPS full spectra in Fig. S17a† shows a new peak of F 1s and an enhanced peak of O 1s owing to the presence of Nafion, as compared to the initial NiPc–GO sample. High-resolution XPS spectra of Ni 2p in Fig. S17b† reveal negligible differences in the binding energy or intensity ratio of Ni^{2+} (855.1 eV) and Ni^{3+} (855.9 eV) in the Ni $2p_{3/2}$ peak. In general, except for the inevitable reduction of oxygen-containing groups on GO, the NiPc–0.4GO as a CO_2RR catalyst exhibits exceptional structural and compositional stability.

To explore the performance differences between NiPc, GO, and NiPc–0.4GO, we test the CV curves and EIS of NiPc and NiPc–0.4GO, as displayed in Fig. 6. The CV curves in Fig. 6a reveal that NiPc–0.4GO exhibits a larger redox area than NiPc. At a potential of >0.5 V *vs.* RHE, NiPc–0.4GO shows a higher oxidation current and a bigger oxidation area than NiPc, indicating higher electrochemical activity.[40] Fig. 6b and S18† show that the NiPc–GO composites have lower impedance than pure NiPc, indicating that GO in NiPc–GO can promote the surface charge transfer. The impedance order of different samples is completely consistent with their FE_{CO}, and NiPc–0.4GO has the lowest impedance. According to the structural evolution of NiPc–GO composites with varying GO amounts, the results reveal that the heterojunction structure between NiPc and GO reduces the interfacial resistance.[41] Excessive GO or NiPc is detrimental to the electron transfer in NiPc–GO. Furthermore, the CV curves of NiPc and NiPc–0.4GO are measured at different scan rates in the non-faradaic region to investigate their double-layer capacitance (C_{dl}) obtained by fitting the scan rate and 1/2 current density (see Fig. S19†).[52] As shown in Fig. 6c, the C_{dl} of NiPc–0.4GO (0.79 mF cm^{-2}) is ~1.6 times than that of NiPc (0.49 mF cm^{-2}). It also demonstrates that NiPc–0.4GO has a larger electrochemical active surface area (ESCA) than NiPc (see Fig. S20†).[52] Fig. 6d proves that the TOF of NiPc–0.4GO is ~1.8 times that of NiPc at various potentials. The above results

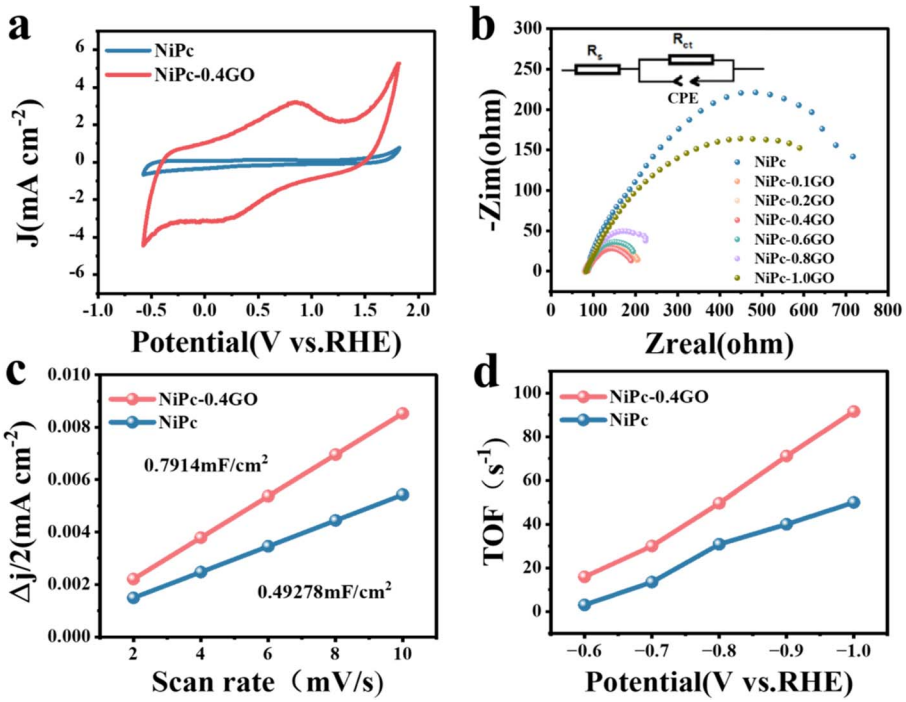

Fig. 6 (a) Cyclic voltammograms of NiPc and NiPc–0.4GO. (b) EIS data for different NiPc–GO composites and NiPc. (c) Linear plots of the 1/2 current density difference *versus* scan rate for NiPc–0.4GO and NiPc. (d) TOF plots of NiPc–0.4GO and NiPc at different potentials.

confirm that the heterojunction formation between NiPc and GO in NiPc–GO can not only accelerate electron transfer, but also provide more active sites.

4. Electrocatalytic mechanism of NiPc–0.4GO

Here, the *in situ* DRIFTS spectra of NiPc, NiPc–0.1 GO, NiPc–0.4 GO and NiPc–1.0 GO are investigated to elucidate their differences in the CO_2RR process in the 0.1 M $KHCO_3$ electrolyte, as illustrated in Fig. 7a–c and S21.† The real-time *in situ* DRIFTS spectra are recorded to capture the dynamic changes of adsorbed CO_2 and intermediates. During the CO_2RR process, in the *in situ* DRIFTS spectra, the characteristic intermediates $*CO_L$ and *COOH are typically observed at ~2138 and ~1400 cm^{-1}, alongside the vibrational peaks of adsorbed CO_2 (~2358 cm^{-1}) and H_2O (~1640 cm^{-1}),[53,54] as shown in Fig. 7. When the work potential is –0.9 V *vs.* RHE, these changes in the *in situ* DRIFTS spectra of NiPc and NiPc–0.4GO with time can be obtained (see Fig. 7a, b and S21†). At the beginning of the electrolysis, the vibration peaks related to adsorbed CO_2 and H_2O are first observed at 2358 and 1640 cm^{-1}, respectively. As the reaction time increases, the peak of CO_2 as a reactant becomes weak, while the broad and strong peak of H_2O appears and becomes strong. Three obvious differences between NiPc and NiPc–GO in the *in situ* DRIFTS spectra can be identified. (1) The CO_2 peak becomes stronger in NiPc–GO than in NiPc, implying that GO can promote CO_2 adsorption. (2) A broader and weaker peak of H_2O is observed in NiPc–GO than in NiPc. This suggests that less water is adsorbed on NiPc–GO than on NiPc as it is consumed as a reactant. This means that more water molecules participate in the CO_2RR, and the hydrogen evolution reaction (HER) can be suppressed on NiPc–GO. (3) The peaks of *CO and *COOH intermediates are more pronounced on NiPc–GO compared to NiPc. This confirms that the existence of GO can facilitate the formation of *COOH, which is usually the rate-limited step during the process of CO_2RR to CO. The weak *CO and *COOH peaks on NiPc strongly suggest that the transformation from *COOH to *CO intermediates, and the *CO desorption of should occur very fast on the Ni–N_4 active site.[24]

Furthermore, the changes in the *in situ* DRIFTS spectra of NiPc–GO and NiPc with the work potential, as shown in Fig. 7c, d and S21†, reveal that higher potential is helpful for both the formation of *COOH intermediates in CO_2RR and the H_2O adsorption on the cathode surface. Fig. 7c clearly presents that the intensity ratio of the *COOH peak to the H_2O peak reaches the maximum at –0.9 V *vs.* RHE, suggesting that the optimal potential for CO_2RR should be –0.9 V. The result is consistent with our experiments. In addition, the peak of the $*CO_L$ intermediate increases with the increase in the *COOH peak, confirming that the *COOH is a key intermediate for CO production. To further reveal the role of GO in the CO_2RR process, the *in situ* DRIFTS spectra of NiPc, NiPc–0.1 GO, NiPc–0.4 GO and NiPc–1.0 GO at –0.9 V *vs.* RHE are also compared, as illustrated in Fig. 7d. When using the intensity of the H_2O peak as a reference at –0.9 V *vs.* RHE, it is evident that with the GO increase in NiPc–GO composites, the intensity ratios of $*CO_2$ to H_2O (I_{*CO_2}/I_{H_2O}) are enhanced, while the I^*_{COOH}/I_{H_2O} ratio of NiPc–0.4GO reaches the maximum. Based on these differences,

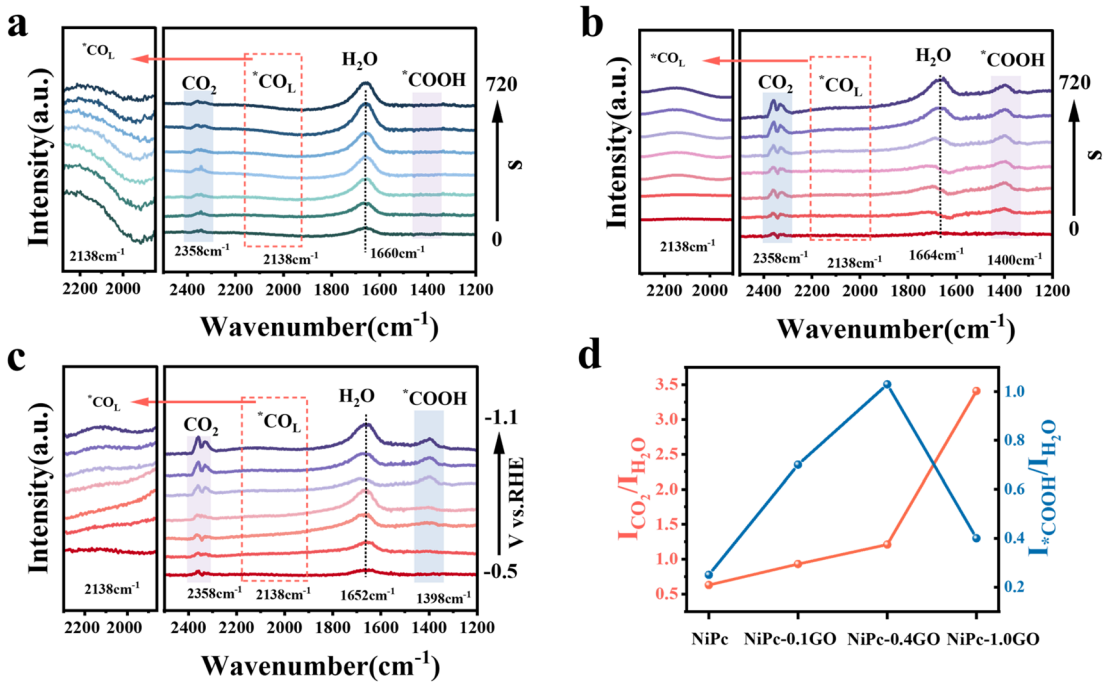

Fig. 7 Time-dependent *in situ* DRIFTS spectra of (a) NiPc and (b) NiPc–0.4GO samples for CO_2RR at −0.9 V *vs.* RHE. (c) *In situ* DRIFTS spectra of NiPc–0.4GO at different work potentials. (d) Change in the I_{CO_2}/I_{H_2O} and I_{*COOH}/I_{H_2O} ratios in *in situ* DRIFTS spectra of NiPc, NiPc–0.1GO, NiPc–0.4GO, and NiPc–1.0GO at −0.9 V *vs.* RHE.

it can be inferred that during the CO_2RR process, GO in the NiPc–GO composites can promote the adsorption of CO_2 and the formation of *COOH intermediates. These advantages of GO can overcome the biggest weakness of NiPc.

To further reveal the relationship between the structure and CO_2RR activity of NiPc–GO samples, the Ni^{2+}/Ni^{3+} ratios in different samples are analysed through the Ni $2p_{3/2}$ XPS spectra, as shown in Fig. 8, S22† and Table S3.† Fig. 8a clearly reveals that no Ni^{3+} can be found in the NiPc sample, and no Ni^{2+} can be identified in NiPc–1.0 GO. With the increase in GO amount in NiPc–GO composites, the ratio of Ni^{2+}/Ni^{3+} decreases from 3.04 to 0.13. This result strongly indicates that NiPc molecules prefer dispersion on the surface of GO through Ni(III)-O-C axial coordination bonds rather than intermolecular π–π stacking during the synthesis process of NiPc–GO composites. As a result, when GO is abundant, all the NiPc molecules should be dispersed as single molecule as observed in the NiPc–1.0GO composite. It can be found that the Ni^{2+}/Ni^{3+} ratio is ~1.11 in NiPc–0.4GO, suggesting that its structure should be a nearly perfect Ni(II)Pc/Ni(III)Pc/GO heterojunction structure. A higher Ni^{2+}/Ni^{3+} ratio indicates the formation of more NiPc aggregates, while a lower ratio implies the existence of more Ni(III)Pc single molecules on GO. As depicted in Fig. 8b, the FE_{CO} and J_{CO} reach the maximum values when the Ni^{3+}/Ni^{2+} ratio is ~1.0, confirming that the Ni(II)Pc/Ni(III)Pc/GO heterojunction structure is the most conductive to CO_2RR. This should be the key reason why the NiPc–0.4GO sample has the best activity for CO_2RR to CO. Neither NiPc aggregates nor single-molecules on GO are favourable for the CO_2RR process. Based on the experiments conducted in this work, the formation and CO_2RR mechanism of NiPc–GO composites can be illustrated in Fig. 8c. After hydrolysis of protonated NiPc in the GO-assisted aqueous system, the generated NiPc can be dispersed on GO through π–π interactions, hydrogen bonding and axial coordination between NiPc and GO. Consequently, the NiPc molecules first cover the GO surface to form the Ni(III) Pc/GO structure. The subsequently generated NiPc molecules will adsorb on Ni(III)Pc/GO through the intermolecular π–π interaction of NiPc, leading to the generation of the Ni(II)/Ni(III)/GO heterojunction structure. More generated NiPc molecules will result in the generation of 2D aggregates of NiPc crystals in the GO-assisted nucleation and growth processes. The graphene-based heterojunction structure of Ni(II)/Ni(III)/GO enhances both the stability and adequate exposure of Ni–N–C active sites for the CO_2 reduction reaction. Additionally, it facilitates efficient electron transfer from the cathode and graphene to NiPc, and the active sites due to the presence the built-in electric field. When the NiPc–GO composite with the Ni(II)/Ni(III)/GO structure act as the CO_2RR catalyst, the electrocatalytic process of CO_2RR to CO involves the CO_2 adsorption, and the generation and desorption of *COOH and *CO intermediates. The cathodic electrons can quickly transfer from ITO and GO to NiPc *via* the axial Ni–O–C bond in the heterojunction. The dissolved CO_2 molecules are preferentially adsorbed and activated to $*CO_2$ on GO, and then the *COOH intermediates form after the proton–electron coupling of $*CO_2$. The generated *COOH on GO can migrate to the Ni sites in Ni(II)Pc, and are quickly protonated to produce *CO intermediates. Finally, the *CO intermediates desorb from the Ni sites to generate CO.

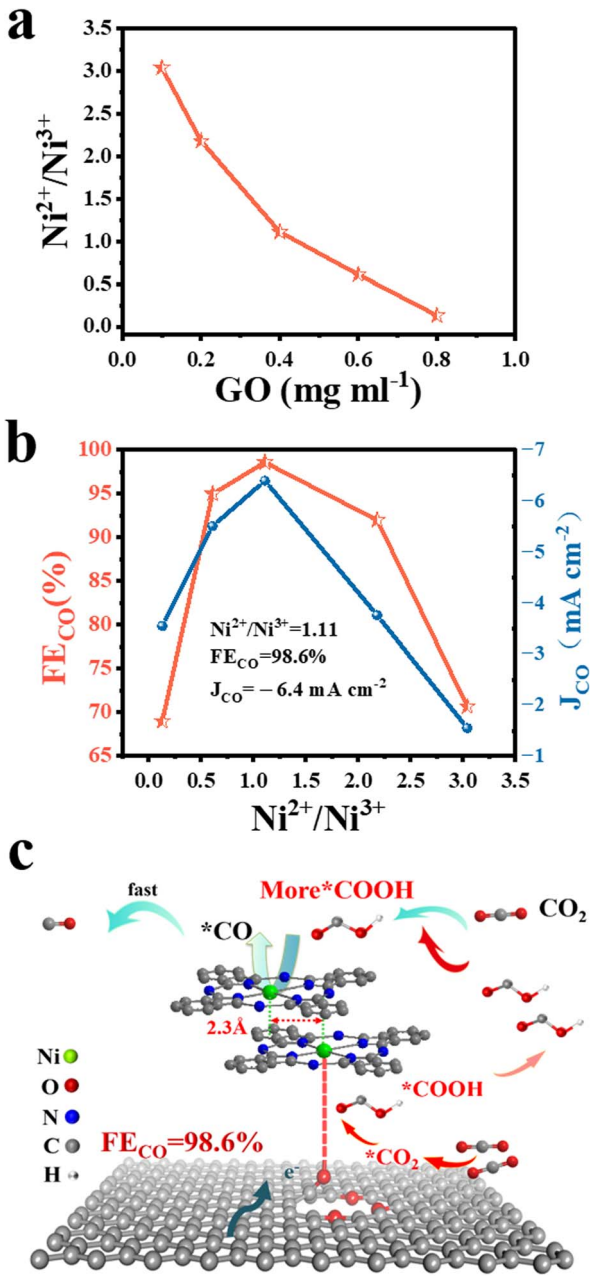

Fig. 8 (a) The variation of FE_{CO}/J_{CO} with the Ni^{2+}/Ni^{3+} ratio at a potential of −0.9 V_{RHE}. (b) The linear correlation between the mass concentration of GO and the Ni^{3+}/Ni^{2+} ratio in NiPc–0.1GO, NiPc–0.2GO, NiPc–0.4GO, NiPc–0.6GO, NiPc–0.8GO, and NiPc–1.0GO. (c) Catalytic mechanism of NiPc–0.4GO in CO_2 reduction.

5. Conclusions

In conclusion, we have successfully developed a non-pyrolysis method to synthesize Ni–N_4 SACs. By changing the mass ratio of NiPc and GO, NiPc molecules with intrinsic Ni–N_4 moieties can be controllably dispersed on GO during the hydrolysis process of protonated NiPc in the GO-assisted aqueous system at room temperature. As the GO content decreases, the evolution of NiPc from single molecules to dimer and then to 2D aggregates can be clearly observed on GO. Systematic characterizations showed that this phenomenon can be attributed to π–π stacking, hydrogen bonding, and axial coordination interactions between NiPc and GO. The optimized NiPc–GO sample exhibits a FE_{CO} of 98.6% at −0.9 V *vs.* RHE and a FE_{CO} of > 90% in the potential range between −0.8 and −1.1 V *vs.* RHE. *In situ* DRIFTS tests clearly verified that GO in NiPc–GO facilitated the CO_2 adsorption and formation of *COOH intermediates, while the inherent Ni–N_4 sites ensured rapid *CO desorption. The change in the Ni^{2+}/Ni^{3+} ratios with varying GO amounts in different NiPc–GO samples further confirmed their structural differences, revealing that the Ni(II)Pc/Ni(III)Pc/GO structure is the most conductive to the CO_2RR process. This work provides a profound understanding of the design and application of metal phthalocyanine in metal–N_4 SACs for the electrocatalytic CO_2RR.

Data availability

The data supporting this article have been included as part of the ESI.†

Conflicts of interest

The authors declare no conflict of interest.

Acknowledgements

This work was supported by the National Nature Science Foundation of China (No. 21705150 and No. 21473204) and the Science and Technology Planning Project of Fujian Province (Grant No. 2014H2008).

References

1 T. Tang, Z. Wang and J. Guan, *Adv. Funct. Mater.*, 2022, **32**, 2111504.
2 Y. Guo, S. Yao, Y. Xue, X. Hu, H. Cui and Z. Zhou, *Appl. Catal., B*, 2022, **304**, 120997.
3 T. Neves-Garcia, M. Hasan, Q. Zhu, J. Li, Z. Jiang, Y. Liang, H. Wang, L. M. Rossi, R. E. Warburton and L. R. Baker, *J. Am. Chem. Soc.*, 2024, **146**, 31633–31646.
4 J. Li, Q. Zhu, A. Chang, S. Cheon, Y. Gao, B. Shang, H. Li, C. L. Rooney, L. Ren, Z. Jiang, Y. Liang, Z. Feng, S. Yang, L. Robert Baker and H. Wang, *Nat. Nanotechnol.*, 2025, DOI: 10.1038/s41565-025-01866-8.
5 Y. Wang, P. Zhu, R. Wang, K. C. Matthews, M. Xie, M. Wang, C. Qiu, Y. Liu, H. Zhou, J. H. Warner, Y. Liu, H. Wang and G. Yu, *ACS Nano*, 2024, **18**, 26751–26758.
6 R. Purbia, S. Y. Choi, C. H. Woo, J. Jeon, C. Lim, D. K. Lee, J. Y. Choi, H.-S. Oh and J. M. Baik, *Appl. Catal., B*, 2024, **345**, 123694.
7 Y.-L. Yang, Q. Li, P. Liu, Q. Xu, Q.-Y. Zeng, Y.-X. Chen, Y.-Q. Yang, H.-T. Yang, F. Yu, Y.-R. Wang, Y. Chen and Y.-Q. Lan, *Adv. Mater.*, 2025, **37**, 2415799.
8 L. Han, S. Song, M. Liu, S. Yao, Z. Liang, H. Cheng, Z. Ren, W. Liu, R. Lin, G. Qi, X. Liu, Q. Wu, J. Luo and H. L. Xin, *J. Am. Chem. Soc.*, 2020, **142**, 12563–12567.

9 F. Wang, Y. Li, X. Xia, W. Cai, Q. Chen and M. Chen, *Adv. Energy Mater.*, 2021, **11**, 2100667.
10 T. Wang, Q. Zhao, Y. Fu, C. Lei, B. Yang, Z. Li, L. Lei, G. Wu and Y. Hou, *Small Methods*, 2019, **3**, 1900210.
11 M. Dunwell, Q. Lu, J. M. Heyes, J. Rosen, J. G. Chen, Y. Yan, F. Jiao and B. Xu, *J. Am. Chem. Soc.*, 2017, **139**, 3774–3783.
12 L. Jiao, C. Mao, F. Xu, X. Cheng, P. Cui, X. Wang, L. Yang, Q. Wu and Z. Hu, *Small*, 2023, **20**, 2305513.
13 Y.-L. Li, X.-L. Jiang, H. Cao, H.-Y. Zhao, J. Li and Y.-G. Wang, *ACS Catal.*, 2024, **14**, 9575–9585.
14 X. Yang, J. Cheng, X. Xuan, N. Liu and J. Liu, *ACS Sustain. Chem. Eng.*, 2020, **8**, 10536–10543.
15 W. Zhang, A. Mehmood, G. Ali, H. Liu, L. Chai, J. Wu and M. Liu, *Angew. Chem., Int. Ed.*, 2025, e202424552.
16 Z. Fan, R. Luo, Y. Zhang, B. Zhang, P. Zhai, Y. Zhang, C. Wang, J. Gao, W. Zhou, L. Sun and J. Hou, *Angew. Chem., Int. Ed.*, 2023, **62**, e202216326.
17 Y. Tan, J. Fu, T. Luo, K. Liu and M. Liu, *J. Am. Chem. Soc.*, 2025, **147**, 4937–4944.
18 X. Zhang, Y. Wang, M. Gu, M. Wang, Z. Zhang, W. Pan, Z. Jiang, H. Zheng, M. Lucero, H. Wang, G. E. Sterbinsky, Q. Ma, Y.-G. Wang, Z. Feng, J. Li, H. Dai and Y. Liang, *Nat. Energy*, 2020, **5**, 684–692.
19 Y. Zhang, L. Jiao, W. Yang, C. Xie and H.-L. Jiang, *Angew. Chem., Int. Ed.*, 2021, **60**, 7607–7611.
20 C. Li, W. Ju, S. Vijay, J. Timoshenko, K. Mou, D. A. Cullen, J. Yang, X. Wang, P. Pachfule, S. Brückner, H. S. Jeon, F. T. Haase, S. C. Tsang, C. Rettenmaier, K. Chan, B. R. Cuenya, A. Thomas and P. Strasser, *Angew. Chem., Int. Ed.*, 2022, **61**, e202114707.
21 M.-K. Hu, N. Wang, D.-D. Ma and Q.-L. Zhu, *Nano Res.*, 2022, **15**, 10070–10077.
22 X. Sui, H. Yuan and Y. Hou, *J. Mater. Chem. A*, 2025, **13**, 638–644.
23 D. Hursán, J. Timoshenko, E. Ortega, H. S. Jeon, M. Rüscher, A. Herzog, C. Rettenmaier, S. W. Chee, A. Martini, D. Koshy and B. Roldán Cuenya, *Adv. Mater.*, 2024, **36**, 2307809.
24 C. Lv, K. Huang, Y. Fan, J. Xu, C. Lian, H. Jiang, Y. Zhang, C. Ma, W. Qiao, J. Wang and L. Ling, *Nano Energy*, 2023, **111**, 108384.
25 J. Wang, K. Zhang, T. T. T. Nga, Y. Wang, Y. Shi, D. Wei, C.-L. Dong and S. Shen, *Chin. J. Catal.*, 2024, **64**, 54–65.
26 Y. Choi, K.-W. Kim, B. J. Park, T. Y. Kim, Y. Lee, B. Park, J. K. Kim and J. W. Han, *J. Mater. Chem. A*, 2025, **13**, 4861–4869.
27 K. Chen, M. Cao, G. Ni, S. Chen, H. Liao, L. Zhu, H. Li, J. Fu, J. Hu, E. Cortés and M. Liu, *Appl. Catal., B*, 2022, **306**, 121093.
28 J. Chen, J. Li, J. Xu, M. Zhu and Y.-F. Han, *Green Energy Environ.*, 2023, **8**, 444–451.
29 K. Chen, M. Cao, Y. Lin, J. Fu, H. Liao, Y. Zhou, H. Li, X. Qiu, J. Hu, X. Zheng, M. Shakouri, Q. Xiao, Y. Hu, J. Li, J. Liu, E. Cortés and M. Liu, *Adv. Funct. Mater.*, 2022, **32**, 2111322.
30 K. Hu, S. Jia, B. Shen, Z. Wang, Z. Dong and H. Lyu, *Chem. Eng. J.*, 2024, **497**, 154686.
31 J.-H. Wu, J.-W. Wang, B. M. Aramburu-Trošelj, F.-J. Niu, L.-J. Guo and G. Ouyang, *Nanoscale*, 2024, **16**, 11496–11512.
32 J. Song, X. Lei, J. Mu, J. Li, X. Song, L. Yan and Y. Ding, *Small*, 2023, **19**, 2305666.
33 J. Guo, X. Yan, Q. Liu, Q. Li, X. Xu, L. Kang, Z. Cao, G. Chai, J. Chen, Y. Wang and J. Yao, *Nano Energy*, 2018, **46**, 347–355.
34 Z. Y. Li, N. P. Young, M. Di Vece, S. Palomba, R. E. Palmer, A. L. Bleloch, B. C. Curley, R. L. Johnston, J. Jiang and J. Yuan, *Nature*, 2008, **451**, 46–48.
35 T. Shimizu, K. Wakamatsu, Y. Yamada, Y. Toyoda, S. Akine, K. Yoza and H. Yoshikawa, *ACS Appl. Mater. Interfaces*, 2021, **13**, 40612–40617.
36 J. Li, S. Wang, R. Li, B. Zhang, X. Xu, Z. Wang and L. Kang, *Appl. Catal., B*, 2024, **342**, 123381.
37 Y. Takahashi, K. Hayakawa, K. Takayama, S. Yokokura, J. Harada, H. Hasegawa and T. Inabe, *Chem. Mater.*, 2014, **26**(2), 993–998.
38 H. Guo, D. H. Si, H. J. Zhu, Z. A. Chen, R. Cao and Y. B. Huang, *Angew. Chem., Int. Ed.*, 2024, **63**, e202319472.
39 Y. Pan, S. Liu, K. Sun, X. Chen, B. Wang, K. Wu, X. Cao, W.-C. Cheong, R. Shen, A. Han, Z. Chen, L. Zheng, J. Luo, Y. Lin, Y. Liu, D. Wang, Q. Peng, Q. Zhang, C. Chen and Y. Li, *Angew. Chem., Int. Ed.*, 2018, **57**, 8614–8618.
40 X. Li, G. Chai, X. Xu, J. Liu, Z. Zhong, A. Cao, Z. Tao, W. You and L. Kang, *Carbon*, 2020, **167**, 658–667.
41 Y. He, Z. Wang, A. Cao, X. Xu, J. Li, B. Zhang and L. Kang, *J. Colloid Interface Sci.*, 2023, **638**, 123–134.
42 M.-D. Zhang, D.-H. Si, J.-D. Yi, S.-S. Zhao, Y.-B. Huang and R. Cao, *Small*, 2020, **16**, 2005254.
43 Y. Choi, K.-W. Kim, B. J. Park, T. Y. Kim, Y. Lee, B. Park, J. K. Kim and J. W. Han, *J. Mater. Chem. A*, 2025, **13**, 4816–4869.
44 K. Hu, S. Jia, B. Shen, Z. Wang, Z. Dong and H. Lyu, *Chem. Eng. J.*, 2024, **497**, 154686.
45 H. Li, K. Gan, R. Li, H. Huang, J. Niu, Z. Chen, J. Zhou, Y. Yu, J. Qiu and X. He, *Adv. Funct. Mater.*, 2022, **33**, 2208622.
46 P. Guo, S. Cao, W. Huang, X. Lu, W. Chen, Y. Zhang, Y. Wang, X. Xin, R. Zou, S. Liu and X. Li, *Adv. Mater.*, 2024, **36**, 2311766.
47 J. Zhao, J. Chen, M. Zhou, Q. Zhang, X. Li and J. Pan, *Chem. Eng. J.*, 2024, **488**, 151110.
48 D.-D. Wu, H.-X. Zhang, Z.-Y. Wang, Y.-L. Zhang and Y.-Z. Wang, *New Carbon Mater.*, 2023, **38**, 1035–1049.
49 S. Shao, S. Xing, K. Bi, T. Zhao, H. Wang, Y. Tang, J. Liu and F. Wang, *Chem. Eng. J.*, 2024, **494**, 152976.
50 W. Li, H. Tang, D. Zhang, T. Huang and B. Xing, *Environ. Sci. Technol.*, 2024, **58**, 5963–5973.
51 Z. Wang, Y. Han, B. Li, P. Peng and S. Q. Zang, *Small*, 2023, **19**, 2301797.
52 S. Min, X. Xu, J. He, M. Sun, W. Lin and L. Kang, *Small*, 2024, **20**, 2400592.
53 J. Han, Q. Xu, F. Tian, H. Sun, Y. Qi, G. Zhang, J.-S. Qin and H. Rao, *Chem. Sci.*, 2024, **15**, 15670–15678.
54 Q. Hao, H.-x. Zhong, J.-z. Wang, K.-h. Liu, J.-m. Yan, Z.-h. Ren, N. Zhou, X. Zhao, H. Zhang, D.-x. Liu, X. Liu, L.-w. Chen, J. Luo and X.-b. Zhang, *Nat. Synth.*, 2022, **1**, 719–728.

